

# Electric-Field-Controlled Thermal Switch in Ferroelectric Materials Using First-Principles Calculations and Domain-Wall Engineering

Chenhan Liu,<sup>1,2</sup> Yunfei Chen,<sup>2</sup> and Chris Dames<sup>1,\*</sup>

<sup>1</sup>*Mechanical Engineering, University of California, Berkeley, Berkeley, California 94720, USA*  
<sup>2</sup>*Jiangsu Key Laboratory for Design and Manufacture of Micro-Nano Biomedical Instruments, School of Mechanical Engineering, Southeast University, Nanjing 211100, P. R. China*

(Received 31 October 2018; revised manuscript received 30 December 2018; published 1 April 2019)

Ferroelectric materials are potential candidates for solid-state thermal switches since their polarizations, interatomic force constants, and microstructures can be tuned by applying an electric field. However, recent experiments on lead zirconate titanate [Ihlefeld et al., *Nano Lett.* 15, 1791–1795 (2015)] and bismuth ferrite [Ning et al., *Phys. Rev. Appl.* 8, 054049 (2017)] thin films only observed weak dependence of thermal conductivity  $k$  on an electric field. In order to explain the experimental results and theoretically explore the electric field-controlled thermal switch, we solve the linearized Boltzmann transport equation with first-principles force constants to calculate  $k$  of  $\text{PbTiO}_3$  at different electric fields. For a single-domain structure, the  $k$  variation under an electric field is caused by the intrinsic structural response, whose main effects are manifested through the phonon-phonon scattering. The  $k$  accumulation function indicates that in order to observe the intrinsic electric field (**E**) effects, the domain size  $d$  should be larger than the critical domain size (CDS), around 30 nm at 300 K and 150 nm at 80 K. Introducing domain wall (DW) scattering creates an additional, extrinsic mechanism for  $k$  control: the effects of an **E** on  $d$  can either increase or decrease the  $k$  variation, and the  $k(T)$  function generally exhibits a peak at some temperature  $T < 300$  K due to the competition between phonon-phonon scattering and DW scattering. This study identifies three strategies to maximize the  $k$  variation in response to an **E**: using samples with  $d$  larger than the CDS, maximizing the sensitivity of  $d$  to an **E**, and decreasing  $T$  to an optimum.

DOI: 10.1103/PhysRevApplied.11.044002

## I. INTRODUCTION

Thermal switches [1,2] are attracting more and more attention due to their potential impacts on diverse applications from thermal management of electronics [3,4] to building energy efficiency [5] and the cold-start of vehicle engines [6]. The most important metric of a thermal switch is its switching ratio, which is defined as the ratio of the on-state thermal conductivity (or conductance) to the off-state value [1]. Compared to liquid-based and gap-based thermal switches [7,8], solid-state thermal switches [9–11], which simply vary their thermal conductivity  $k$  at the atomic scale, are appealing due to their simplicity and potential compactness.

Ferroelectric (FE) materials [12] are potential candidates for high switching ratios among solid-state thermal switches due to their different structures below and above the temperature  $T$  of the phase transition. For example, molecular dynamics simulation showed that the switch ratio of polyethylene nanofibers can reach 6 at the phase transition [13]. However, thermal switches based on  $T$ -induced phase transition only work at the phase transition

temperature, which will limit their applications. In FE materials, the phase transition can also be triggered by a sufficiently strong external electric field (**E**), even away from the zero-field transition  $T$ . This suggests that **E** effects in FE materials may be an efficient way to modulate  $k$  and realize a high switching ratio across a range of  $T$ . Based on this mechanism, a first-principles calculation found that the **E**-controlled thermal switch based on  $\text{BaTiO}_3$  (BTO) may have a best-case switching ratio of 9.4 [14] by changing from a paraelectric cubic phase to a ferroelectric rhombohedral phase.

Apart from **E**-induced phase transitions, **E**-induced domain wall (DW) scattering through changing DW density is another mechanism to realize  $k$  switching in FE materials, since DWs can significantly scatter phonons [15–17]. For example, experimentally, at very low  $T$  (approximately 10 K), Mante and Volger [15] observed a fourfold increase of  $k$  in BTO under an **E** due to the reduction in DW density and scattering. A recent nonequilibrium Green's function calculation at room  $T$  also showed that a DW of 0.4-nm thickness can reflect 37% of the phonon energy, a fraction that increases to 59% if the DW thickness triples [16]. However, for bilayer lead zirconate titanate (PZT) thin film (or membrane PZT film)

\*cdames@berkeley.edu

at 300 K, time-domain thermoreflectance (TDTR) measurement indicated DW scattering only induces 10% [10] (or 13% [18])  $k$  variation under  $\mathbf{E}$ . In a BiFeO<sub>3</sub> (BFO) thin film, another recent TDTR measurement [19] could not observe any variation of  $k$  under an  $\mathbf{E}$ , although the DW density varied significantly. These disagreements between the theoretical calculations and experimental measurements and even among the experiments are puzzling. The discrepancies could arise from effects of residual and/or substrate strain, different domain sizes, defects, impurities, or even simply the different FE materials used. To resolve this conflict, it would be helpful to have a more detailed understanding of the phonon behavior in these FE materials than is accessible in those experiments. To this end, we calculate  $k$  with the linearized Boltzmann transport equation (BTE) and obtain detailed information such as the mean-free-path-dependent accumulated  $k$ .

PbTiO<sub>3</sub> (PTO) is a prototypical FE material, which has only one phase transition around 760 K [12], transforming from a cubic to a tetragonal phase. Below 760 K, PTO retains the tetragonal phase all the way down to 0 K, which simplifies the analysis compared to other FE materials having more than one phase transition. PTO has only five atoms in the unit cell, which is advantageous for  $k$  calculation. PTO is also of fundamental interest because it is one end member of many important FE solid solutions such as PbZr<sub>x</sub>Ti<sub>1-x</sub>O<sub>3</sub> and  $x$ PbMg<sub>1/3</sub>Nb<sub>2/3</sub>O<sub>3</sub>-(1- $x$ )PbTiO<sub>3</sub>. Therefore, PTO is chosen as the model material to investigate  $k$  variation under an  $\mathbf{E}$ .

A first-principles method with the linearized BTE is applied to investigate the  $\mathbf{E}$  effects on  $k$  of PTO. The

details of applying an  $\mathbf{E}$  can be found in Refs. [14,20,21] and the Appendix. Throughout this work, the  $\mathbf{E}$  is applied along the [001] direction, that is, the polarization direction, and  $k$  is evaluated along the in-plane direction [100]. We note that the  $\mathbf{E}$  effects on  $k$  along [001] are similar to those along [100]. The simulation is performed at 0 K using the VASP package [22]. For a single-domain structure at 300 K, we find that  $\mathbf{E} = 1000$  kV/cm can cause a 16% variation of  $k$ , and the variation increases as  $T$  decreases. In order to observe the  $\mathbf{E}$ -induced  $k$  variation, the domain size should exceed the critical domain size (CDS) based on the mean-free-path-dependent accumulated  $k$ . For a multidomain structure, we find changing the domain size at different  $\mathbf{E}$  can increase or decrease the  $k$  variation due to the competition between DW scattering and phonon-phonon scattering.

## II. RESULTS AND DISCUSSION

Figure 1(a) shows the calculated polarization hysteresis loop of PTO, with simulation details given in the Appendix. Because the hysteresis loop is multivalued and covers all four quadrants, in the thermal conductivity results below, it is important to unambiguously identify the corresponding state of the hysteresis loop. In this work, all the thermal conductivity results are discussed referring to the lower branch of Fig. 1(a), indicated by the states labeled D-A-C-B, primarily focusing on A ( $\mathbf{E} = -2000$  kV/cm,  $\mathbf{P} = -116 \mu\text{C}/\text{cm}^2$ ) and B (2000 kV/cm,  $-74 \mu\text{C}/\text{cm}^2$ ). Note that  $\mathbf{E}$  and  $\mathbf{P}$  are parallel for state A, while  $\mathbf{E}$  and  $\mathbf{P}$  are antiparallel for state B.

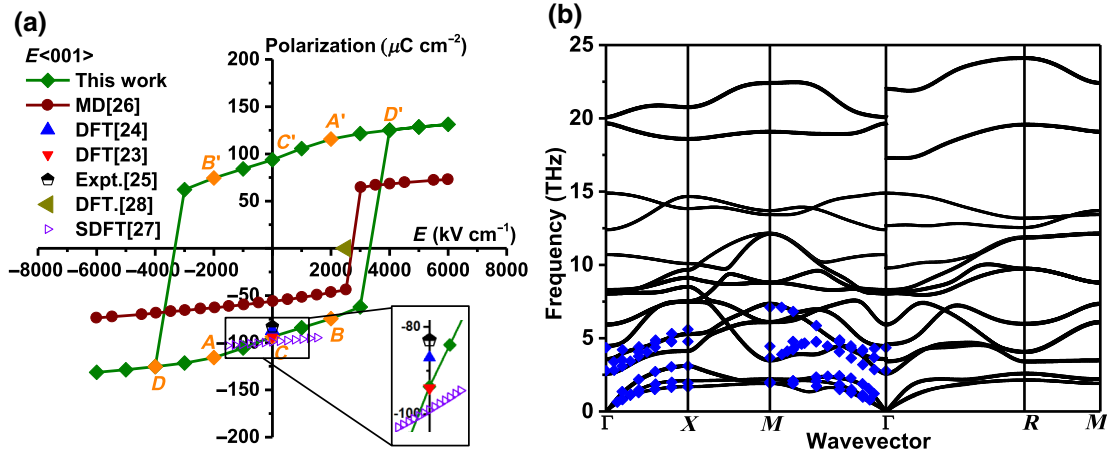


FIG. 1. (a) The polarization hysteresis loop in PTO at  $T=0$  K unless otherwise noted. Due to the symmetry, state A ( $\mathbf{E} = -2000$  kV/cm,  $\mathbf{P} = -116 \mu\text{C}/\text{cm}^2$ ) and state B ( $\mathbf{E} = 2000$  kV/cm,  $\mathbf{P} = 74 \mu\text{C}/\text{cm}^2$ ) have counterparts  $A'$  ( $\mathbf{E} = 2000$  kV/cm,  $\mathbf{P} = 116 \mu\text{C}/\text{cm}^2$ ) and  $B'$  ( $\mathbf{E} = -2000$  kV/cm,  $\mathbf{P} = -74 \mu\text{C}/\text{cm}^2$ ). The green diamond points represent this work. The brown circles are from an MD simulation at 100 K based on a shell model potential [26], the unfilled purple triangles are from SPDF [27] simulation, and the dark yellow triangle is from a first-principles calculation (2500 kV/cm) based on the internal energy landscape using the fixed-dielectric-displacement approach [28]. The spontaneous polarization ( $94 \mu\text{C}/\text{cm}^2$ ) of this work is close to previous DFT calculations [23,24] (red and blue triangle points) and experimental data [25] at 300 K (black pentagon). (b) The calculated phonon dispersion of PTO at zero field. The blue diamond points are from experimental data [35].

Furthermore, due to the symmetries of the hysteresis loop, point  $A$  has counterpart  $A'$ , and similarly  $B \leftrightarrow B'$ , and so on, as indicated, and clearly  $k(A) = k(A')$ ,  $k(B) = k(B')$ , and so on.

The calculated spontaneous polarization at state  $C$  is very close to previous first-principles calculations and experimental data [23–25]. The dependence of polarization on  $\mathbf{E}$  at  $T=0$  K (green diamonds,  $T=0$  K unless otherwise noted) is similar to that from molecular dynamics simulation at 100 K based on a shell model potential [26] (brown circles) and from second-principles density-functional theory [27] (SPDFT) simulation (purple triangles). From Fig. 1(a), the polarization reversal happens at the coercive field  $\mathbf{E}_C$  between 3000 and 4000 kV/cm, which is close to a previous molecular dynamics simulation (2700 kV/cm) at 100 K [26] and first-principles calculation (2500 kV/cm) based on the internal energy landscape using the fixed-dielectric-displacement approach [28], but much higher than the experimental value (approximately 10 kV/cm) at room temperature [29,30].

As we discussed in detail in Ref. [14], this large discrepancy in the coercive field between experiment and first-principles calculations is an artifact arising from the fact that the first-principles calculations are based on a single unit cell calculation at 0 K, which thereby lacks the thermal energy and nucleation sites that greatly ease the polarization reversal in real materials at higher temperatures [31–34]. First-principles calculations are still accurate for determining the polarization, as seen by the very good agreement with experiments for spontaneous polarization in Fig. 1(a) and in similar calculations of BaTiO<sub>3</sub> in Fig. 5(a) of Ref. [14]. Importantly, for understanding thermal conductivity, we argue that polarization is a more appropriate physical metric than  $\mathbf{E}$ , because the structure is determined by the atomic configuration, which corresponds to  $\mathbf{P}$  rather than  $\mathbf{E}$ . In other words,  $\mathbf{E}$  and  $T$  together are the stimulus, while  $\mathbf{P}$  represents the actual structural response. Nevertheless, because ferroelectric behavior is more conventionally discussed in terms of  $\mathbf{E}$  as the independent variable, we adhere to that convention in this paper in order to make the results more straightforward and comparable with previous research.

Figure 1(b) shows the phonon dispersion of tetragonal PTO at zero field. The blue diamond points are the experimental data [35], which match well with our calculation. The calculation shows several discontinuities around the  $\Gamma$  point along different Brillouin zone directions, because the long range correction near the  $\Gamma$  point is nonanalytic [36,37]. In addition, the relaxed lattice constants ( $a=3.878$  Å,  $c/a=1.082$ ) are also close to the experimental data ( $a=3.88$  Å,  $c/a=1.071$ ) [38] and previous first-principles calculations ( $a=3.87$  Å,  $c/a=1.086$ ) [39].

Applying  $\mathbf{E}$  can lengthen polarization vectors, which are parallel to the  $\mathbf{E}$ , reverse polarizations, which are antiparallel to  $\mathbf{E}$ , and change the DW density. We begin

by analyzing these effects on the thermal conductivity separately by first isolating the effects of structural (polarization) response at constant DW density and then the effects of DW density. In our model, the structural response is reflected in the phonon-phonon scattering while the DW density response is reflected in the DW scattering. We begin with a single-domain structure, that is, structural response, of PTO under an  $\mathbf{E}$ .

Under the linearized Boltzmann transport equation, the phonon thermal conductivity  $k_{\text{ph}}$  is calculated as [40]

$$k_{\text{ph}} = \frac{1}{k_B T^2 \Omega N} \sum_{\lambda} f_0 (f_0 + 1) (\hbar \omega_{\lambda} v_{\lambda})^2 \tau_{\lambda}, \quad (1)$$

$$\frac{1}{\tau_{\lambda}} = \frac{1}{\tau_{\lambda,p}} + \frac{1}{\tau_{\lambda,o}}, \quad (2)$$

$$\frac{1}{\tau_{\lambda,o}} = \frac{\pi \omega^2}{2N} \sum_{\lambda'} \sum_{i \in u.c.} g(i) |\mathbf{e}_{\lambda}^*(i) \cdot \mathbf{e}_{\lambda'}(i)|^2 \delta(\omega_{\lambda} - \omega_{\lambda'}), \quad (3)$$

where  $k_B$ ,  $T$ ,  $\Omega$ ,  $N$ ,  $f_0$ ,  $\omega$ ,  $v$ ,  $\lambda$ ,  $u.c.$ , and  $\mathbf{e}$  are the Boltzmann constant, temperature, volume of unit cell, number of wave vector points, equilibrium Bose-Einstein distribution, phonon frequency, phonon group velocity, phonon mode (wave vector and branch), unit cell, and the normalized eigenvector, respectively. In Eq. (3),  $g(i)$  is the Pearson deviation coefficient of atomic mass describing the isotopic effects [40]. The total scattering time  $\tau_{\lambda}$  of Eqs. (1) and (2) in the single-domain structure is composed of phonon-phonon scattering  $\tau_{\lambda,p}$  and isotopic scattering  $\tau_{\lambda,o}$  based on Matthiessen's rule. Both scattering phenomena can be calculated without any fitting parameters [40], thus  $k$  calculation for the single-domain structure has no fitting errors. As a convergence check,  $k$  with cut-off distances of 4 and 4.5 Å are calculated independently and their difference is less than 1.8%, thus 4 Å is applied in the calculations below to reduce the computational cost. Additional simulation details are given in the Appendix.

Figure 2(a) shows the resulting calculated  $k$  of single-domain PTO as a function of  $T$  at different  $\mathbf{E}$ . At zero field (state  $C$ ), our results are in very good agreement with a previous first-principles calculation [41] and have some difference compared to experimental data [42]. Above 200 K, the experimental  $k$  is higher than our calculation. Previous first-principles work [41] has attributed a similar underestimation of experimental  $k$  to the harmonic approximation in the phonon dispersion and the neglect of electronic thermal conductivity and spin-orbit effect. On the other hand, below 200 K, our calculation overestimates the experimental  $k$ . We believe this is because our model [Eq. (1)] ignores scattering by defects and impurities, which become important at lower  $T$  near the peak of the  $k(T)$  curve. Furthermore, in experiment [42], the PTO sample has complex DW structures, which could contribute significant scattering to phonons [15–17], while DW scattering has been

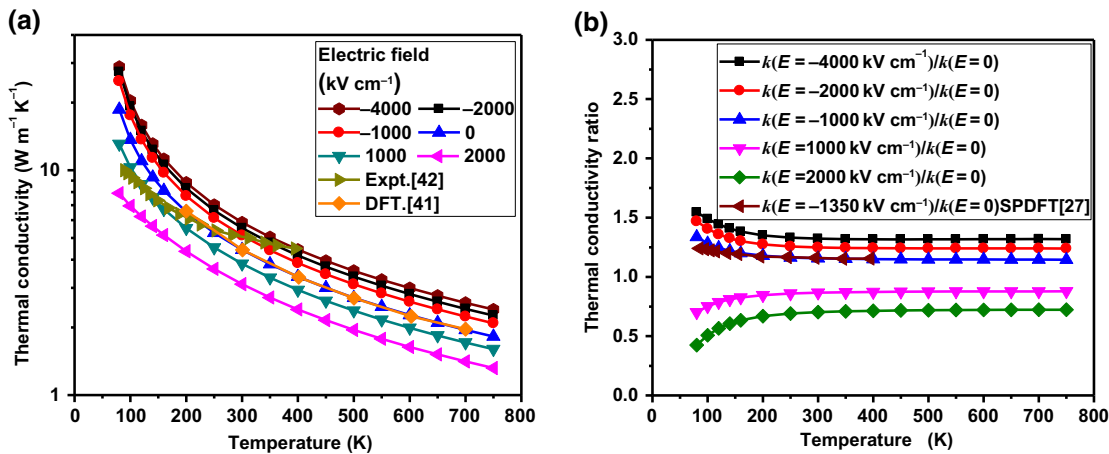


FIG. 2. (a) The thermal conductivity  $k$  of PTO vs  $T$  at different  $\mathbf{E}$ , corresponding to states  $D$  ( $\mathbf{E} = -4000 \text{ kV/cm} \rightarrow A$  ( $\mathbf{E} = 2000 \text{ kV/cm}$ ) of Fig. 1(a)). The rightward dark yellow triangle points are from experimental data [42] and the orange diamond points from a previous first-principles calculation [41] at zero field. (b) The ratio of  $k$  at different  $\mathbf{E}$  to that at zero field (state  $C$ ). The ratio  $k(\mathbf{E} = -1000 \text{ kV/cm})/k(\mathbf{E} = 0)$  (blue triangles) in this work lies close to  $k(\mathbf{E} = -1350 \text{ kV/cm})/k(\mathbf{E} = 0)$  from a recent SPDFT simulation [27] (brown triangles).

ignored in our model so far. Returning to the higher  $T$  regions of Fig. 2(a), for  $T > 350 \text{ K}$ , the simulation results give  $k \propto T^{-0.97}$ , very close to the classic  $T^{-1}$  law for a bulk single-crystalline material dominated by phonon-phonon scattering above the Debye  $T$  (337 K for crystalline PTO [43]).

The ratio of  $k$  at different  $\mathbf{E}$  to that at zero field is shown in Fig. 2(b). In this work,  $k(\mathbf{E} = -1000 \text{ kV/cm})/k(\mathbf{E} = 0)$  across the whole  $T$  range almost coincides with  $k(\mathbf{E} = -1350 \text{ kV/cm})/k(\mathbf{E} = 0)$  from a very recent SPDFT simulation [27], supporting our calculation. From Fig. 2(b), the variation of  $k$  increases with decreasing  $T$ . It is worth mentioning that the  $k$  variation here is caused by the intrinsic structural response under  $\mathbf{E}$  because this is a single-domain calculation, and that the intrinsic structural response mainly affects  $k$  through the phonon-phonon scattering. At 300 K, compared to the initial zero-field reference state ( $\mathbf{P} = -94 \mu\text{C}/\text{cm}^2$ ),  $k$  of PTO decreases by 16% at  $\mathbf{E} = 1000 \text{ kV/cm}$  ( $\mathbf{P} = -84 \mu\text{C}/\text{cm}^2$ ) while increasing 16% at  $\mathbf{E} = -1000 \text{ kV/cm}$  ( $\mathbf{P} = -106 \mu\text{C}/\text{cm}^2$ ).

For PTO, we cannot find any experimental investigations about the  $\mathbf{E}$  effects on  $k$ . The closest related experiments are two recent studies of PZT thin films [10,18], which have some relevance because, as noted above, PTO is an end member of the PZT system. In the bilayer PZT thin film experiment, at 300 K,  $k$  decreases 10% at  $\mathbf{E} = \pm 500 \text{ kV/cm}$  [10], and in the membrane PZT film experiment,  $k$  increases 13% abruptly at  $\mathbf{E} = 100 \text{ kV/cm}$  [18]. Although the  $k$  variation for PTO at 1000 kV/cm found here is similar to that seen in the PZT film experiments [10,18], the reason is different. In our single-domain calculation, the  $k$  variation is caused by an intrinsic structural response (phonon-phonon scattering) while the PZT film

experiments attributed the  $k$  variation to the DW scattering via field-dependent DW density.

Another experiment on BFO thin film [19] showed that the cross-plane  $k$  at  $\pm 2000 \text{ kV/cm}$  has virtually no change ( $<\sim 6\%$ ) compared to 0 kV/cm at 300 K even though the density of DW changes significantly, which means DW scattering has negligible effects on  $k$ , in apparent contradiction of the PZT film experiments. We will discuss the reason for this conflict below around Figs. 3 and 4 by considering the DW effects in our model. However, according to our calculation for single-domain PTO, the intrinsic structural effects on phonon-phonon scattering at the same  $\mathbf{E} = -2000 \text{ kV/cm}$ , that is, state  $A$ , ( $\mathbf{E} = 2000 \text{ kV/cm}$ , that is, state  $B$ ) as the BFO experiment [19] can cause a 25% (30%)  $k$  variation. The reason no  $k$  variation was seen in the BFO thin film experiment [19] might have been due to the effects of substrate strain. This is because two BFO polymorphs (denoted “R-like” and “T-like”) in the experiment were forced by the substrate strain. We note a fundamental similarity between the effects of substrate strain in Ref. [19] and the  $\mathbf{E}$  here, in that both shift the atomic coordinates of the material. As seen here in Fig. 2(a), the response of  $k$  to  $\mathbf{E}$  begins to saturate at high fields. For example, increasing  $\mathbf{E}$  from  $-2000 \text{ kV/cm}$  (state  $A$ ) to  $-4000 \text{ kV/cm}$  (state  $D$ ) only causes a 5.6% difference in  $k$ . Therefore, because in the BFO experiments [19] the atomic coordinates are already forced into a highly strained state by the substrate lattice mismatch, we expect that it is more difficult for the applied  $\mathbf{E}$  to induce much additional strain and thereby further alter  $k$ . Based on this argument, we suggest that in experiments, it is necessary to reduce the residual strain in a sample as much as possible in order to best observe the  $\mathbf{E}$ -induced  $k$  variation.

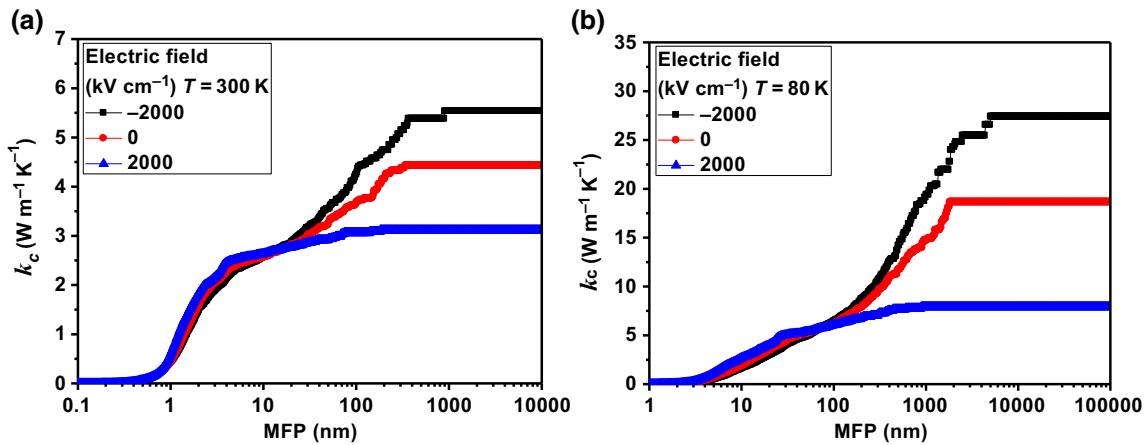


FIG. 3. The cumulative thermal conductivity  $k_c$  with  $\mathbf{E} = -2000 \text{ kV/cm}$  (state *A*:  $\mathbf{P} = -116 \mu\text{C}/\text{cm}^2$ ), 0 (state *C*:  $\mathbf{P} = -94 \mu\text{C}/\text{cm}^2$ ), and  $2000 \text{ kV/cm}$  (state *B*:  $\mathbf{P} = -74 \mu\text{C}/\text{cm}^2$ ), respectively, at  $T = 300 \text{ K}$  (c) and  $80 \text{ K}$  (d) vs phonon MFP. All calculations are for a single-domain sample with natural isotopes concentrations.

As discussed above, different experiments have reached different conclusions about the importance of DW scattering for  $\mathbf{E}$ -modulated  $k$ , considering them variously important (PZT [10,18]) or negligible (BFO [19]). Such experiments cannot provide detailed mode-wise information about phonons in these FE materials to help explain the apparent conflict. Therefore, to shed some light on these detailed scattering interactions, here, for PTO, we calculate the accumulated thermal conductivity  $k_c(\Lambda)$ . In this definition,  $k_c(\Lambda)$  represents the thermal conductivity carried by phonons with mean free paths (MFPs =  $\tau v$ ) less than  $\Lambda$ . The results are shown in Fig. 3. It is interesting to note that this room- $T$   $k_c$  is essentially independent of  $\mathbf{E}$  strength for MFPs below 30 nm. We call this 30 nm the CDS, which means that for samples with domain and/or grain sizes comparable to or smaller than the CDS (thereby truncating the longer MFP contributions),  $\mathbf{E}$  should have virtually no effect on  $k$ . The experiment on BFO thin film [19] does not explicitly provide the domain size information, but the film thickness provided is 30 nm, so we take this as a reasonable estimate of the boundary scattering length, which behaves similar to DW scattering. Therefore, if the  $k_c$  accumulation function for BFO has a CDS comparable to that of PTO as seen in Fig. 3(a), this would be another mechanism that suppresses the intrinsic  $k$  variation with  $\mathbf{E}$ , in addition to the substrate strain effect mentioned above. Thus, it is important to prepare samples with domain and/or grain sizes well above the CDS to best observe the  $\mathbf{E}$  effects on  $k$ . Comparing Figs. 3(a) and 3(b), the CDS is larger (approximately 150 nm) at lower  $T$ , which is expected because of the longer MFPs for intrinsic phonon-phonon scattering.

Even though the substrate strain and CDS effects could explain the null results of the BFO experiment, the apparent contradiction of DW scattering effects on  $k$  among the available literature experiments remains

unclear. Moreover, our calculation is based on an infinitely large single-domain structure, while the experimental samples have many domains. In order to further explore the contradiction and bring our calculations closer to the practical experimental conditions, we generalize the total scattering time  $\tau$  (that is,  $\tau_\lambda$ , but now suppressing the  $\lambda$  for compactness of notation) in Eqs. (1) and (2) using Matthiessen's rule as follows

$$\frac{1}{\tau} = \frac{1}{\tau_p} + \frac{1}{\tau_i} + \frac{1}{\tau_d} = \frac{1}{\tau_p} + A\omega^4 + \frac{\nu}{d}, \quad (4)$$

where  $\tau_p$  is the phonon-phonon scattering time,  $\tau_i$  is a Rayleigh-like scattering time by impurities, defects, and isotopes, and  $\tau_d$  is the DW scattering time. Here,  $\tau_p$  is calculated as  $\tau_{\lambda p}$  in the single-domain structure case [40], but  $\tau_i$  is different from  $\tau_{\lambda i}$  in Eq. (3) since the isotope scattering is combined with impurity and defect scattering as the Rayleigh-like scattering and is treated by fitting below. Regarding  $\tau_d$ , recent nonequilibrium Green's function calculations showed DW can scatter phonons across almost the whole frequency range [16]. The results indicated that at 300 K, 37% of the phonon energy is reflected by a DW of 0.4-nm thickness, and the reflected energy increases to 59% if the DW thickness triples. Furthermore, Weilert *et al.* [17] experimentally and theoretically showed that DWs act as nearly perfect grain boundaries in the ferroelectric potassium dihydrogen phosphate (KDP) in accordance with acoustic mismatch theory. Therefore, we use the simple relationship  $\tau_d^{-1} = \nu/d$ , where  $d$  is the representative domain size. This form is adapted from a widely used model of grain boundary scattering [44–52] and corresponds to phonon scattering by, on average, once per domain. It is worth mentioning that  $\nu$  is a function of phonon frequency and polarization (longitudinal acoustic branch, transverse optical branch, etc.) through

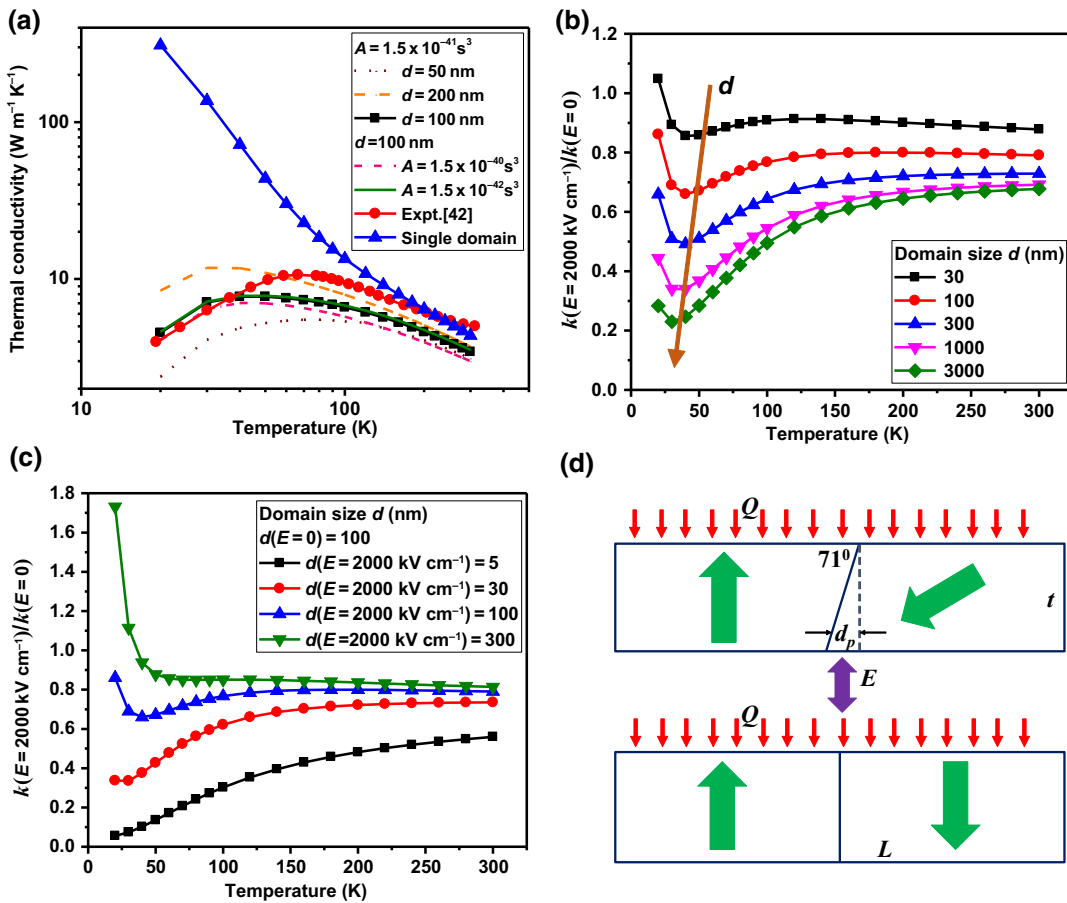


FIG. 4. (a) The thermal conductivity of PTO using the fitted multidomain model (purple, light yellow, black, pink, and green lines), single-domain model (blue triangle points), and experiment (red circle points) [42], all at zero field [state C of Fig. 1(a)]. The fitted value in Eq. (4) is  $d = 100 \text{ nm}$  and  $A = 1.5 \times 10^{-41} \text{ s}^3$ . The fitted multidomain profile (black square points) matches much better with the experimental data (red circle points) than does the single-domain calculation (blue triangle points), with an overall rms residual error decreasing from 1786% to 26%. (b) The ratio of  $k$  at  $\mathbf{E} = 2000 \text{ kV/cm}$  (state B) to that at  $\mathbf{E} = 0$  with  $d = 30, 100, 300, 1000, 3000 \text{ nm}$ , respectively. The domain sizes for both  $\mathbf{E}$  are same. The arrow highlights how the optimized  $T$  for minimized  $k$  ratio (largest  $k$  variation) decreases with increasing  $d$ . (c) The ratio of  $k$  at  $\mathbf{E} = 2000 \text{ kV/cm}$  with  $d = 5, 30, 100, 300 \text{ nm}$ , respectively, to  $k$  at  $\mathbf{E} = 0$  with fixed  $d = 100 \text{ nm}$ . (d) The switchable evolution of R-like BFO domain under  $\mathbf{E}$ , following ref. [19]. Under the cross-plane  $\mathbf{E}$  (top), a 71° DW emerges, while for  $\mathbf{E} = 0$  (bottom), the DW relaxes toward the cross-plane direction.  $L$  is the in-plane domain size,  $t$  is the film thickness, and  $d_p$  is the projection of the 71° DW along the in-plane direction.

the phonon mode index  $\lambda$ , so that these DW scattering rates are actually evaluated using  $\tau_{d,\lambda}^{-1} = v_\lambda/d$  in a more complete notation.

We fix the parameters  $A$  and  $d$  of Eq. (4) by fitting experimental  $k(T)$  data from the literature [42]. As shown in Fig. 4(a), the best-fit values are  $d = 100 \text{ nm}$  and  $A = 1.5 \times 10^{-41} \text{ s}^3$ . This value of  $A$  is similar to that extracted from experimental  $k(T)$  for 5% oxygen vacancies LaLuO<sub>3</sub> ( $A = 1-2 \times 10^{-41} \text{ s}^3$ ) [53]. Figure 4(a) shows that across the  $T$  range 20–300 K, the  $k(T)$  model considering DW and Rayleigh-like scatterings (black square points) is much better than the previous single-domain calculation (blue triangle points) at matching the experimental data (red circle points), with an overall rms residual error decreasing from 1786% (blue vs red points) to 26% (black vs red points).

Next, we fix the parameter  $A$  (Rayleigh-like scattering) and explore the effects of  $d$  (DW scattering) on  $k$  with  $\mathbf{E}$ . Figure 4(b) shows the ratio of  $k$  at  $\mathbf{E} = 2000 \text{ kV/cm}$  (state B) to that at  $\mathbf{E} = 0$  (state C) for various  $d$  from 30 to 3000 nm. In Fig. 4(b), we assume  $d$  remains same for the two  $\mathbf{E}$ s, that is, when assessing the numerator and denominator of the  $k$  ratio. From Fig. 4(b), it is clear that for a given  $T$ , a larger  $d$  allows larger  $k$  variation, that is, greater  $k$  suppression at  $\mathbf{E} = 2000 \text{ kV/cm}$ . For example, at 300 K, the  $k$  variation increases from 12% to 32% (almost three times) as  $d$  increases from 30 to 3000 nm. This is because the CDS effect makes  $k$  less sensitive to  $\mathbf{E}$  for small  $d$ . On the other hand, as  $d$  increases, the DW scattering becomes weaker and phonon-phonon scattering becomes dominant, revealing the effects of  $\mathbf{E}$  on intrinsic phonon-phonon scattering.

Figure 4(b) also shows that as  $T$  decreases, the sensitivity of  $k$  to  $d$  first increases and then decreases, with a peak at some  $T$ , for example, approximately 40 K for  $d = 300$  nm, and the peak shifts to lower  $T$  for larger  $d$ . This is due to the competition between phonon-phonon scattering (increasingly important at high  $T$ ) and DW scattering (takes over at low  $T$ ). To explain in more detail, as indicated in Fig. 2(b), the  $k$  variation should increase at low  $T$  due to an intrinsic structural response. However, at low  $T$ , the DW scattering dominates the heat transport and its rates  $v/d$  at different  $\mathbf{E}$ s (same  $d$ ) are similar, which limits the CDS effect and predicts a small  $k$  variation. Thus, it is reasonable that the  $k$  variation has a peak and the peak moves to lower  $T$  for larger  $d$ . For the structure with  $d = 3000$  nm,  $k$  has a maximum change of about 77% under 2000 kV/cm at 30 K. In this case, the switch ratio is 4.3, which should be large enough to be easily measured in an experiment if such a large-domain sample could be prepared.

The above discussion assumes the same  $d$  at different  $\mathbf{E}$ . In reality, the  $\mathbf{E}$  can change the  $d$  significantly [15,19]. In order to describe the additional effects of  $d$  change on  $k$ , we now compare the ratio of  $k$  at  $\mathbf{E} = 2000$  kV/cm (state  $B$ ) and  $d = 5, 30, 100, 300$  nm, respectively, to a reference case of  $\mathbf{E} = 0$  (state  $C$ ) and  $d$  fixed at 100 nm. The results are shown in Fig. 4(c), which indicates that the largest effects of  $\mathbf{E}$  on  $k$  (black squares) come from simultaneously increasing  $\mathbf{E}$  and decreasing  $d$  [that is, transitioning from states  $D \rightarrow A \rightarrow C \rightarrow B$  in Fig. 1(a)]. Qualitatively, this is fully expected from the previous simulations. We have already seen that  $[\partial k / \partial \mathbf{E}]_d < 0$  throughout this  $\mathbf{E}$  range from the intrinsic phonon-phonon scattering effects [e.g., Figs. 2, 3, and 4(b)], and obviously  $[\partial k / \partial d]_{\mathbf{E}} > 0$  [Eq. (4)]. Then if  $[\partial d / \partial \mathbf{E}] < 0$ , which is the case for the red and black data series of Fig. 4(c), we see that increasing  $\mathbf{E}$  tends to decrease  $k$  both directly through the increased phonon-phonon scattering and indirectly through stronger DW scattering. Quantitatively, Fig. 4(c) indicates that, for example, if a 2000 kV/cm field decreases  $d$  from 100 nm (blue triangles) to 5 nm (black squares), the  $k$  variation at 300 K will increase from 21% to 44%, and from 23% to 70% at 100 K. The corresponding switch ratios are 1.8 at 300 K and 3.3 at 100 K, which is a large value for a solid-state thermal switch. Similarly, for  $\mathbf{E} = -2000$  kV/cm [state  $A$  of Fig. 1(a)], we can infer that increasing (decreasing) the domain size under  $\mathbf{E}$  can increase (decrease) the  $k$  variation, as verified by a calculation analogous to Fig. 4(c), but using  $\mathbf{E} = -2000$  kV/cm (details omitted for brevity).

Figure 4(c) also shows that the  $k$  sensitivity to  $\mathbf{E}$  first increases and then decreases with decreasing  $T$ . As in Fig. 4(b), this again is due to the CDS effect and the competition between phonon-phonon scattering and DW scattering. Interestingly, at  $T$  lower than 30 K with  $d = 300$  nm (green triangle points),  $k$  at  $\mathbf{E} = 2000$  kV/cm is larger than that

at  $\mathbf{E} = 0$ , while the relation is opposite at  $T$  higher than 30 K. That is because at low  $T$ , DW scattering dominates the heat transport and  $k$  is determined simply by  $d$ . In that case, we can simply predict that larger  $d$  causes larger  $k$ .

According to the above discussions, when the domain and/or grain size is smaller than the CDS,  $k$  is dominated by the domain and/or grain boundary scattering and is not directly sensitive to  $\mathbf{E}$ . On the other hand, for domain and/or grain size larger than the CDS, the effects of intrinsic structural response on phonon-phonon scattering emerge and  $k$  becomes sensitive to  $\mathbf{E}$ . Apart from the possible substrate strain effects discussed above, this distinction could also help explain the apparent contradiction between the BFO [19] and PZT thin-film [10] experiments. For the BFO thin-film experiment, the switchable evolution of the  $R$ -like BFO domain under  $\mathbf{E}$  is indicated schematically in Fig. 4(d). The films have thickness  $t = 30$  nm. An average in-plane domain size may be estimated as  $L > 100$  nm from the piezoresponse-force microscopy at zero field [19]. Due to the  $\mathbf{E}$  alignment effects,  $L$  will increase under  $\mathbf{E}$  and we assume it doubles to  $L > 200$  nm under the strong  $\mathbf{E}$  (2000 kV/cm) applied in this paper. The paper shows that under  $\mathbf{E}$ , the large surface area electrode can stabilize to a 71° tilt domain, but does not clearly show the angle between the domain and in-plane direction. Here, we assume the angle is 71° as indicated in Fig. 4(d, top).

Accordingly, we now present a simple geometric argument to estimate the potential impact of these 71° domains. For a given domain of in-plane extent  $L^2$ , the projected area of the DW along four sides is approximately  $4Ld_p$ , where  $d_p = t/\tan(71^\circ)$  is the projected area of the DW normal to the heat flux direction. After dividing by 2 to avoid double counting effects, the 71° domain wall can only influence 10% (i.e.,  $2t/L\tan 71^\circ$ ) of the area ( $L^2$ ). Thus, 90% of the heat transporting across the thin film is not affected by the 71° DW. For the  $T$ -like BFO (180° domain wall), the DW is always parallel to the heat transport direction both with and without  $\mathbf{E}$ . Thus, for both  $T$ -like and  $R$ -like BFO thin films, for these specific geometries, the DW scattering is not important. In addition, the thin-film thickness is only 30 nm (below the CDS), so that the structural response is also unimportant. Therefore, because the film is so thin, the overall heat transport is simply dominated by boundary scattering at the top and bottom of the 30-nm BFO film, which makes it difficult to observe the cross-plane  $k$  variation under a cross-plane  $\mathbf{E}$ . However, for the PZT thin film experiment [10], the thickness is 200 nm and  $d$  (average size is 30 nm) is changed by approximately 10% upon applying the  $\mathbf{E}$ . More importantly, the DW angle is 90°, thus the DW scattering is dominant and leads to the  $k$  variation, albeit only by a scale comparable to the variation in  $d$ , which is consistent with our calculation.

### III. CONCLUSION

The thermal conductivity of PTO as a function of  $\mathbf{E}$  is calculated from a first-principles method with the linearized Boltzmann transport equation. For a single-domain structure, the  $k$  variation with  $\mathbf{E}$  becomes stronger at lower  $T$  and arises mainly from the effects of the intrinsic structural response (atomic strain) on the phonon-phonon scattering. The mean-free-path-accumulated thermal conductivity indicates that in order to maximize the effects of  $\mathbf{E}$  on  $k$ , the domain size should be larger than a CDS, which is approximately 30 nm at 300 K and increases to approximately 150 nm at 80 K. By introducing DW scattering, we find that changing the domain size can increase or decrease the  $k$  variation depending on whether the  $\mathbf{E}$  tends to increase or decrease the DW density. Finally, we identify three strategies to maximize the switchability of  $k$  in response to  $\mathbf{E}$ : using samples with domain sizes larger than the CDS, maximizing the sensitivity of domain size to  $\mathbf{E}$ , and decreasing  $T$  to an optimum that is well below 300 K.

### ACKNOWLEDGMENTS

This research used the Savio computational cluster resource provided by the Berkeley Research Computing program at the University of California, Berkeley (supported by the UC Berkeley Chancellor, Vice Chancellor for Research, and Chief Information Officer). The authors thank Geoff Wehmeyer for helpful comments. Y.C. acknowledges the financial support from the National Key R&D Program of China (Grant No. 2017YFB0406000). C.L. is supported by the Scientific Research Foundation of Graduate School of Southeast University (Grant No. YBJJ1541) and the Fundamental Research Funds for the Central Universities and the Innovative Project for Graduate Students of Jiangsu Province (Grant No. KYLX15\_0058). C.L. also acknowledges financial support from the China Scholarship Council (Grant No. CSC-201606090029).

C.L. and C.D. initiated the project. C.L. carried out the calculations and wrote the manuscript. Y.C. and C.D. supervised the project. C.L., Y.C., and C.D. edited the manuscript. All authors discussed the results and commented on the manuscript.

### APPENDIX: FIRST-PRINCIPLES METHOD TO APPLY ELECTRIC FIELD

The first-principles calculations of the structural response in this work follow Fu and Bellaiche [20], as detailed in Ref. [14]. Here, we briefly outline some key simulation details, and refer the reader to Ref. [14] for additional information. The structure minimizes the

electric enthalpy functional [20,21]

$$F(\mathbf{R}, \boldsymbol{\eta}, \mathbf{E}) = U_{\text{KS}}[\mathbf{R}(\mathbf{E}), \boldsymbol{\eta}(\mathbf{E})] - \mathbf{E} \cdot \mathbf{P}(\mathbf{R}, \boldsymbol{\eta}, \mathbf{E}), \quad (\text{A1})$$

with force constraint

$$\mathbf{Q}_{\text{HF}}^i = -\mathbf{E} \cdot \mathbf{Z}_i^*(\mathbf{R}, \boldsymbol{\eta}, \mathbf{E}), \quad (\text{A2})$$

where  $F$  is the electric enthalpy,  $U_{\text{KS}}$  is the Kohn-Sham energy at atomic coordinates  $\mathbf{R}$  and strain  $\boldsymbol{\eta}$  of the unit cell,  $\mathbf{E}$  is the electric field,  $\mathbf{P}$  is the polarization,  $\mathbf{Q}_{\text{HF}}^i$  is the Hellmann-Feynman force, and  $\mathbf{Z}_i^*$  is the Born effective charge tensor. We developed an iterative procedure [14] to obtain the structure under  $\mathbf{E}$  (Fig. 5, same as Fig. 1 of Ref. [14]). Step 1, initialize the simulation with atomic coordinates and strain (beginning from the values already found from a previous  $\mathbf{E}$ ). Step 2, use the Vienna Ab-initio Simulation Package (VASP) [22] and a conjugate-gradient algorithm to relax atoms under the new  $\mathbf{E}$  [Eq. (A1)] with force constraint [Eq. (A2)]. Step 3, compare relaxed coordinates and strain with those of previous iteration and iterate until differences are smaller than their respective tolerances  $\epsilon_1$  (0.0001 Å) and  $\epsilon_2$  (0.01%).

The DFT energy cut off of the plane wave basis set is 600 eV with the projector augmented wave (PAW) pseudopotentials [54]. The generalized gradient approximation (GGA) of revised Perdew-Burke-Ernzerhof [55] (PBE) is applied for the electronic exchange-correlation interaction. The  $5d^{10} 6s^2 6p^2$ ,  $3s^2 3p^6 3d^2 4s^2$ ,  $2s^2 2p^4$  are treated as valence electrons in Pb, Ti, and O atoms, respectively. A  $10 \times 10 \times 10$  Monkhorst-Pack  $K$  points

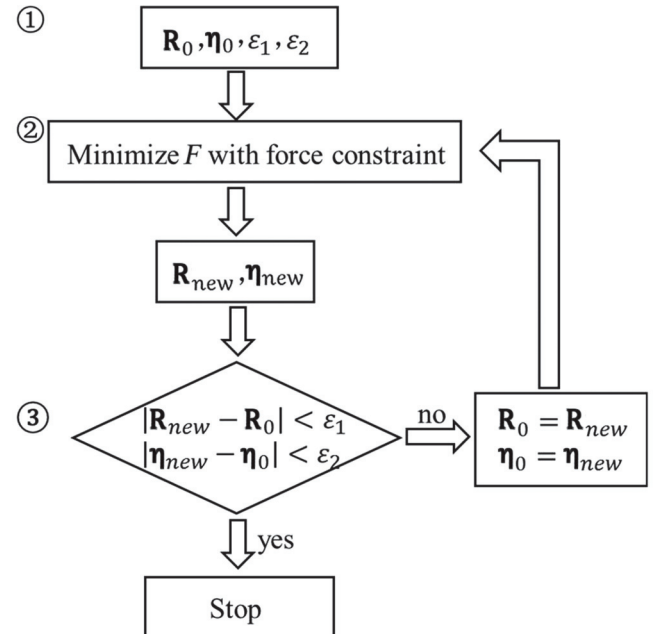


FIG. 5. Iteration method to obtain the converged structure of PTO under  $\mathbf{E}$ . The three numbered steps are discussed in the text.

mesh is sampled for structural relaxation and the force tolerance is 0.001 eV/Å. A  $4 \times 4 \times 4$  supercell is used to calculate the second-order force constants and a  $3 \times 3 \times 3$  supercell to calculate the third-order force constants. The Born effective charge and dielectric constant tensors are calculated by the Berry phase theory [56] in order to account for long-range electrostatic interactions, which are important in polar materials [37,57,58]. Then the second-order force constants, Born effective charge, and dielectric constant tensors are applied to calculate the phonon dispersion with the Phonopy package [59]. Finally, the in-plane [100] direction thermal conductivity is obtained by solving the linearized Boltzmann transport equation implemented in the ShengBTE package [40], using a  $20 \times 20 \times 20$  wavevector mesh and a 0.40-nm cut-off distance for the third-order force constants. We confirm reasonable numerical convergence for this ShengBTE step by comparing  $16 \times 16 \times 16$  wavevector meshing and 0.45-nm cutoff distance, which changes the resulting  $k$  values by only 3%.

- 
- [1] G. Wehmeyer, T. Yabuki, C. Monachon, J. Q. Wu, and C. Dames, Thermal diodes, regulators, and switches: Physical mechanisms and potential applications, *Appl. Phys. Rev.* **4**, 041304 (2017).
- [2] B. W. Li, L. Wang, and G. Casati, Thermal Diode: Rectification of Heat Flux, *Phys. Rev. Lett.* **93**, 184301 (2004).
- [3] T. Y. Yang, B. Kwon, P. B. Weisensee, J. G. Kang, X. J. Li, P. Braun, N. Miljkovic, and W. P. King, Millimeter-scale liquid metal droplet thermal switch, *Appl. Phys. Lett.* **112**, 063505 (2018).
- [4] R. Bosisio, S. Valentini, F. Mazza, G. Benenti, R. Fazio, V. Giovannetti, and F. Taddei, Magnetic thermal switch for heat management at the nanoscale, *Phys. Rev. B* **91**, 205420 (2015).
- [5] W. Chun, Y. J. Ko, H. J. Lee, H. Han, J. T. Kim, and K. Chen, Effects of working fluids on the performance of a bi-directional thermodiode for solar energy utilization in buildings, *Sol. Energy* **83**, 409 (2009).
- [6] K. Dahal, Q. Zhang, Y. M. Wang, I. K. Mishra, and Z. F. Ren, V-VO<sub>2</sub> core-shell structure for potential thermal switching, *RSC Adv.* **7**, 33775 (2017).
- [7] M. Leriche, S. Harmand, M. Lippert, and B. Desmet, An experimental and analytical study of a variable conductance heat pipe: Application to vehicle thermal management, *Appl. Therm. Eng.* **38**, 48 (2012).
- [8] J. Cho, C. Richards, D. Bahr, J. Jiao, and R. Richards, Evaluation of contacts for a MEMS thermal switch, *J. Micromech. Microeng.* **18**, 105012 (2008).
- [9] G. H. Zhu, J. Liu, Q. Y. Zheng, R. G. Zhang, D. Y. Li, D. Banerjee, and D. G. Cahill, Tuning thermal conductivity in molybdenum disulfide by electrochemical intercalation, *Nat. Commun.* **7**, 13211 (2016).
- [10] J. F. Ihlefeld, B. M. Foley, D. A. Scrymgeour, J. R. Michael, B. B. McKenzie, D. L. Medlin, M. Wallace, S. Trolier-McKinstry, and P. E. Hopkins, Room-temperature voltage tunable phonon thermal conductivity via reconfigurable interfaces in ferroelectric thin films, *Nano Lett.* **15**, 1791 (2015).
- [11] C. Y. Tso and C. Y. H. Chao, Solid-state thermal diode with shape memory alloys, *Int. J. Heat. Mass Transf.* **93**, 605 (2016).
- [12] K. M. Rabe, C. H. Ahn, and J.-M. Triscone, *Physics of Ferroelectrics: A Modern Perspective* (Springer, Berlin; New York, 2007).
- [13] T. Zhang and T. F. Luo, High-contrast, reversible thermal conductivity regulation utilizing the phase transition of polyethylene nanofibers, *ACS Nano* **7**, 7592 (2013).
- [14] C. H. Liu, V. Mishra, Y. F. Chen, and C. Dames, Large thermal conductivity switch ratio in barium titanate under electric field through first-principles calculation, *Adv. Theory Simul.* **30**, 248 (2016).
- [15] A. J. H. Mante and J. Volger, Phonon transport in barium titanate, *Physica* **52**, 577 (1971).
- [16] M. Royo, C. Escorihuela-Sayalero, J. Iniguez, and R. Rurrali, Ferroelectric domain wall phonon polarizer, *Phys. Rev. Mater.* **1**, 051402 (2017).
- [17] M. A. Weilert, M. E. Msall, A. C. Anderson, and J. P. Wolfe, Phonon-Scattering from Ferroelectric Domain-Walls - Phonon Imaging in KDP, *Phys. Rev. Lett.* **71**, 735 (1993).
- [18] B. M. Foley, M. Wallace, J. T. Gaskins, E. A. Paisley, R. L. Johnson-Wilke, J. W. Kim, P. J. Ryan, S. Trolier-McKinstry, P. E. Hopkins, and J. F. Ihlefeld, Voltage-controlled bistable thermal conductivity in suspended ferroelectric thin-film membranes, *ACS Appl. Mater. Interfaces* **10**, 25493 (2018).
- [19] S. Ning, S. C. Huberman, C. Zhang, Z. J. Zhang, G. Chen, and C. A. Ross, Dependence of the Thermal Conductivity of BiFeO<sub>3</sub> Thin Films on Polarization and Structure, *Phys. Rev. Appl.* **8**, 054049 (2017).
- [20] H. X. Fu and L. Bellaiche, First-Principles Determination of Electromechanical Responses of Solids Under Finite Electric Fields, *Phys. Rev. Lett.* **91**, 057601 (2003).
- [21] L. Chen, Y. R. Yang, and X. K. Meng, Giant electric-field-induced strain in lead-free piezoelectric materials, *Sci. Rep.* **6**, 25346 (2016).
- [22] G. Kresse and J. Furthmüller, Efficiency of ab-initio total energy calculations for metals and semiconductors using a plane-wave basis set, *Comput. Mater. Sci.* **6**, 15 (1996).
- [23] R. K. Behera, C. W. Lee, D. Lee, A. N. Morozovska, S. B. Sinnott, A. Asthagiri, V. Gopalan, and S. R. Phillpot, Structure and energetics of 180 degrees domain walls in PbTiO<sub>3</sub> by density functional theory, *J. Phys.: Condens. Matter* **23**, 175902 (2011).
- [24] Y. J. Wang, Y. L. Zhu, and X. L. Ma, Chiral phase transition at 180 degrees domain walls in ferroelectric PbTiO<sub>3</sub> driven by epitaxial compressive strains, *J. Appl. Phys.* **122**, 134104 (2017).
- [25] Y. Liu, Y. L. Zhu, Y. L. Tang, Y. J. Wang, Y. X. Jiang, Y. B. Xu, B. Zhang, and X. L. Ma, Local Enhancement of polarization at PbTiO<sub>3</sub>/BiFeO<sub>3</sub> interfaces mediated by charge transfer, *Nano Lett.* **17**, 3619 (2017).
- [26] X. W. Zeng and R. E. Cohen, Thermo-electromechanical response of a ferroelectric perovskite from molecular dynamics simulations, *Appl. Phys. Lett.* **99**, 142902 (2011).

- [27] J. A. Seijas-Bellido, H. Aramberri, J. Iniguez, and R. Rurali, Electric control of the heat flux through electrophononic effects, *Phys. Rev. B* **97**, 184306 (2018).
- [28] J. W. Hong and D. Vanderbilt, Mapping the energy surface of  $\text{PbTiO}_3$  in multidimensional electric-displacement space, *Phys. Rev. B* **84**, 115107 (2011).
- [29] M. Wang, G. L. Tan, and Q. J. Zhang, Multiferroic properties of nanocrystalline  $\text{PbTiO}_3$  ceramics, *J. Am. Ceram. Soc.* **93**, 2151 (2010).
- [30] Z. Nurbaya and M. Rusop, The potential role of amorphous lead titanate thin films as nanodielectric layer for capacitor applications, *IOP Conf. Ser.-Mater. Sci.* **64**, 012055 (2014).
- [31] Y. L. Li, L. E. Cross, and L. Q. Chen, A phenomenological thermodynamic potential for  $\text{BaTiO}_3$  single crystals, *J. Appl. Phys.* **98**, 064101 (2005).
- [32] W. H. Ma and A. Z. Hao, Electric field-induced polarization rotation and ultrahigh piezoelectricity in  $\text{PbTiO}_3$ , *J. Appl. Phys.* **115**, 104105 (2014).
- [33] O. E. Fesenko and V. S. Popov, Phase T,E-diagram of barium-titanate, *Ferroelectrics* **37**, 729 (1981).
- [34] S. J. Ahmed, S. Pichardo, L. Curiel, and O. Rubel, First-principle modelling of the ferroelectric switching in  $\text{BaTiO}_3$ : Concurrent switching versus domain wall motion, *Model. Simul. Mater. Sci. Eng.* **22**, 055014 (2014).
- [35] I. Tomono, Y. Ishii, Y. Tsunoda, and K. Oka, Lattice dynamics of tetragonal  $\text{PbTiO}_3$ , *Phys. Rev. B* **73**, 064116 (2006).
- [36] Y. Wang, S. L. Shang, H. Z. Fang, Z. K. Liu, and L. Q. Chen, First-principles calculations of lattice dynamics and thermal properties of polar solids, *NPJ Comput. Mater.* **2**, 16006 (2016).
- [37] Y. Wang, J. J. Wang, W. Y. Wang, Z. G. Mei, S. L. Shang, L. Q. Chen, and Z. K. Liu, A mixed-space approach to first-principles calculations of phonon frequencies for polar materials, *J. Phys.: Condens. Matter* **22**, 202201 (2010).
- [38] S. A. Mabud and A. M. Glazer, Lattice-parameters and birefringence in  $\text{PbTiO}_3$  single-crystals, *J. Appl. Crystallogr.* **12**, 49 (1979).
- [39] D. I. Bilc, R. Orlando, R. Shaltaf, G. M. Rignanese, J. Iniguez, and P. Ghosez, Hybrid exchange-correlation functional for accurate prediction of the electronic and structural properties of ferroelectric oxides, *Phys. Rev. B* **77**, 165107 (2008).
- [40] W. Li, J. Carrete, N. A. Katcho, and N. Mingo, ShengBTE: A solver of the Boltzmann transport equation for phonons, *Comput. Phys. Commun.* **185**, 1747 (2014).
- [41] A. Roy, Estimates of the thermal conductivity and the thermoelectric properties of  $\text{PbTiO}_3$  from first principles, *Phys. Rev. B* **93**, 100101(R) (2016).
- [42] M. Tachibana, T. Kolodiaznyi, and E. Takayama-Muromachi, Thermal conductivity of perovskite ferroelectrics, *Appl. Phys. Lett.* **93**, 092902 (2008).
- [43] W. N. Lawless, T. Nakamura, M. Takashige, and S. L. Swartz, Specific-heat of amorphous and crystalline  $\text{PbTiO}_3$  at low-temperatures, *J. Phys. Soc. Jpn.* **52**, 207 (1983).
- [44] T. Hori, J. Shiomi, and C. Dames, Effective phonon mean free path in polycrystalline nanostructures, *Appl. Phys. Lett.* **106**, 171901 (2015).
- [45] C. Kang, H. Kim, S. G. Park, and W. Kim, Comparison of thermal conductivity in nanodot nanocomposites and nanograined nanocomposites, *Appl. Phys. Lett.* **96**, 213114 (2010).
- [46] D. M. Rowe and V. S. Shukla, The effect of phonon-grain boundary scattering on the lattice thermal-conductivity and thermoelectric conversion efficiency of heavily doped fine-grained, hot-pressed silicon germanium alloy, *J. Appl. Phys.* **52**, 7421 (1981).
- [47] H. S. Yang, G. R. Bai, L. J. Thompson, and J. A. Eastman, Interfacial thermal resistance in nanocrystalline yttria-stabilized zirconia, *Acta. Mater.* **50**, 2309 (2002).
- [48] A. J. Minnich, H. Lee, X. W. Wang, G. Joshi, M. S. Dresselhaus, Z. F. Ren, G. Chen, and D. Vashaee, Modeling study of thermoelectric SiGe nanocomposites, *Phys. Rev. B* **80**, 155327 (2009).
- [49] H. J. Goldsmid and A. W. Penn, Boundary scattering of phonons in solid solutions, *Phys. Lett. A* **27**, 523 (1968).
- [50] G. Joshi, H. Lee, Y. C. Lan, X. W. Wang, G. H. Zhu, D. Z. Wang, R. W. Gould, D. C. Cuff, M. Y. Tang, M. S. Dresselhaus, G. Chen, and Z. F. Ren, Enhanced thermoelectric figure-of-merit in nanostructured p-type silicon germanium bulk alloys, *Nano Lett.* **8**, 4670 (2008).
- [51] S. K. Bux, R. G. Blair, P. K. Gogna, H. Lee, G. Chen, M. S. Dresselhaus, R. B. Kaner, and J. P. Fleural, Nanostructured bulk silicon as an effective thermoelectric material, *Adv. Funct. Mater.* **19**, 2445 (2009).
- [52] Z. J. Wang, J. E. Alaniz, W. Y. Jang, J. E. Garay, and C. Dames, Thermal conductivity of nanocrystalline silicon: Importance of grain size and frequency-dependent mean free paths, *Nano Lett.* **11**, 2206 (2011).
- [53] E. Langenberg, E. Ferreiro-Vila, V. Leboran, A. O. Fumega, V. Pardo, and F. Rivadulla, Analysis of the temperature dependence of the thermal conductivity of insulating single crystal oxides, *APL Mater.* **4**, 104815 (2016).
- [54] G. Kresse and D. Joubert, From ultrasoft pseudopotentials to the projector augmented-wave method, *Phys. Rev. B* **59**, 1758 (1999).
- [55] J. P. Perdew, A. Ruzsinszky, G. I. Csonka, O. A. Vydrov, G. E. Scuseria, L. A. Constantin, X. L. Zhou, and K. Burke, Restoring the Density-Gradient Expansion for Exchange in Solids and Surfaces, *Phys. Rev. Lett.* **100**, 136406 (2008).
- [56] R. Resta, Macroscopic polarization in crystalline dielectrics - the geometric phase approach, *Rev. Mod. Phys.* **66**, 899 (1994).
- [57] X. Gonze, J. C. Charlier, D. C. Allan, and M. P. Teter, Interatomic force-constants from first principles - the case of alpha-quartz, *Phys. Rev. B* **50**, 13035 (1994).
- [58] A. Togo, L. Chaput, and I. Tanaka, Distributions of phonon lifetimes in Brillouin zones, *Phys. Rev. B* **91**, 094306 (2015).
- [59] A. Togo and I. Tanaka, First principles phonon calculations in materials science, *Scr. Mater.* **108**, 1 (2015).